Touch-induced Mechanical Strain in Somatosensory Neurons is Independent of Extracellular Matrix Mutations in *C. elegans*

Adam L. Nekimken[1,2,†], Beth L. Pruitt[1,2,†,*], and Miriam B. Goodman[1,2,*]

[1]Stanford University Department of Mechanical Engineering

[2]Stanford University Department of Molecular and Cellular Physiology

[†]Current address: Fullmoon Sensors, Inc. (ALN) and University of California-Santa Barbara Department of Mechanical Engineering (BLP)

[*]Corresponding authors: blp@ucsb.edu (BLP) and mbgoodmn@stanford.edu (MBG)

Running Head: Mechanical strain in sensory neurons

Abbreviations:

TRN: touch receptor neuron

ECM: extracellular matrix

Abstract

Cutaneous mechanosensory neurons are activated by mechanical loads applied to the skin, and these stimuli are proposed to generate mechanical strain within sensory neurons. Using a microfluidic device to deliver controlled stimuli to intact animals and large, immobile, and fluorescent protein-tagged mitochondria as fiducial markers in the touch receptor neurons (TRNs), we visualized and measured touch-induced mechanical strain in *C. elegans* worms. At steady-state, touch stimuli sufficient to activate TRNs induce an average strain of 3.1% at the center of the actuator and this strain decays to near zero at the edges of the actuator. We also measured strain in animals carrying mutations affecting links between the extracellular matrix (ECM) and the TRNs but could not detect any differences in touch-induced mechanical strain between wild-type and mutant animals. Collectively, these results demonstrate that touching the skin induces local mechanical strain in intact animals and suggest that a fully intact ECM is not essential for transmitting mechanical strain from the skin to cutaneous mechanosensory neurons.

38 **Introduction**

39 Touch and proprioception are essential to the daily lives of all animals, including
40 humans. Classical examples of mechanotransduction, both of these senses depend on activation
41 of mechano-electrical transduction (MeT) channels arrayed within somatosensory neurons (Katta
42 et al., 2015) and are thought to activate following physical deformation of sensory cells during
43 touch and movement. Consistent with this inference, neurons innervating stretch receptor organs
44 in vertebrates (Bewick and Banks, 2015) and arthropods (Suslak and Jarman, 2015) are activated
45 by experimentally applied mechanical strain (stretch). High-speed volumetric imaging reveals
46 that proprioceptors deform in crawling Drosophila larvae (He et al., 2019; Vaadia et al., 2019)
47 and that physical deformations are correlated with calcium transients. Similarly, movement
48 induces localized calcium transients in the tertiary dendrites of the *C. elegans* PVD
49 proprioceptors that depend on expression of a DEG/ENaC/ASIC protein (Tao et al., 2019). These
50 studies reinforce the idea that physical deformation of sensory neurons during movement is
51 critical for activation of native MeT channels, but do not address whether or not similar
52 deformations occur in response to touch or measure the extent of mechanical strain that occurs
53 within the sensory neurons themselves.

54 Using *C. elegans* touch receptor neurons (TRNs), we investigated the quantitative
55 relationship between touch and physical deformation of sensory neurons in intact living animals.
56 The ready availability of transgenic animals expressing TRN-specific markers and their
57 transparent body make *C. elegans* an especially useful animal for investigating touch-evoked
58 sensory neuron deformation. Adult animals have six TRNs, consisting of two bilaterally
59 symmetric pairs of touch receptor neurons (ALM and PLM) and two neurons that run along the
60 ventral midline (AVM and PVM) (Goodman, 2006). These six neurons extend long, unusually
61 straight sensory neurites (Krieg et al., 2017) that are embedded in epidermal cells and have a
62 distinctive, electron-dense extracellular matrix or ECM as well as hemidesmosome structures
63 attaching the TRNs to the cuticle (Chalfie and Sulston, 1981; Chalfie and Thomson, 1979).

64 All of the TRNs express the MEC-4 channel, which is required for touch-evoked calcium
65 transients (Suzuki et al., 2003) and touch-evoked MeT currents (O'Hagan et al., 2005). The
66 MEC-4 channels localize to puncta arrayed along the entire length of wild-type TRN sensory

67 neurites (Chelur et al., 2002; Cueva et al., 2007; Emtage et al., 2004; Katta et al., 2019), but are
68 disrupted in ECM mutants (Emtage et al., 2004).

69 Touch-evoked behavior (Petzold et al., 2013) and MeT channel activation (Eastwood et
70 al., 2015) depend on body indentation rather than the force applied. Slow stimuli fail to activate
71 MeT currents and their size increases with stimulus frequency, indicating that activation of MeT
72 channels in their native environment depends on tissue viscoelasticity (Eastwood et al., 2015;
73 Katta et al., 2019; Sanzeni et al., 2019). Although slow, movement-induced physical
74 deformations of the worm's body and its neurons are too slow to activate MeT currents in the
75 TRNs (Eastwood et al., 2015; Katta et al., 2019), these undulatory movements produce
76 mechanical strains of up to 40% (Krieg et al., 2017; Krieg et al., 2014), indicating that TRNs can
77 withstand significant mesoscale extension and compression *in situ*. The ability to withstand
78 movement-induced strain is shared by mammalian nerves that experience up to 30% strain
79 during limb movement (Phillips et al., 2004).

80 Here, we sought to determine whether or not body indentations sufficient to evoke
81 calcium transients in TRNs also generate local strain. To achieve this goal, we visualized steady-
82 state, touch-induced strain in TRNs in living animals restrained within a microfluidic stimulation
83 device equipped with the ability to deliver mechanical stimuli (Fehlauer et al., 2018; Nekimken
84 et al., 2017a). Our approach benefits from large, immobile mitochondria distributed within TRN
85 sensory neurites (Sure et al., 2018), exploits the ability to tag these mitochondria with a red
86 fluorescent protein (Zheng et al., 2014), and borrows analytic principles from traction force
87 microscopy (Ribeiro et al., 2016). Although mitochondria have been used to evaluate neuronal
88 mechanics in culture (O'Toole et al., 2015), we believe this study is the first to make use of
89 mitochondria as mechanical fiducial markers in living animals. We show that body indentation
90 increases local steady-state mechanical strain in the TRNs in a manner that is robust to mutations
91 known to affect attachment of the TRN to the extracellular matrix and to epidermal cells.

Results

Mechanical stimulation in a microfluidic device

To directly observe touch-induced deformation of the TRNs, we sought to develop a method that combines the delivery of controlled mechanical stimuli and three-dimensional optical imaging. To reach this goal, we applied mechanical stimuli to adult worms confined in a microfluidic device (Nekimken *et al.*, 2017, Figure 1A). Our device has pneumatic actuators that consist of a thin flexible wall that separates a channel filled with air from a worm in the trap channel. When air pressure in the actuator channel is increased using a pressure controller, the thin wall expands like a balloon, deforming the trapped worm and generating indentations sufficient to activate the TRNs (Nekimken et al., 2017a). Other devices that deliver mechanical stimuli to restrained (Cho et al., 2018) or moving (McClanahan et al., 2017) worms in microfluidic chambers have been reported, but they use larger actuator channels and are thus not well-matched to our goal of investigating local deformation of the TRNs.

Our device is designed to increase the probability that animals will enter the trap with either their left or right sides in contact with the bottom of the chamber and their ventral and dorsal sides near the actuator (Nekimken et al., 2017a). Consistent with this expectation and the position of the AVM and ALM neurons within the worm's body, previous experiments using this device resulted in a higher frequency of AVM activation compared to ALM (Nekimken et al., 2017a). However, the rotational orientation of each worm was variable. We took advantage of this variation to select animals oriented such that ALM (rather than AVM) was near the actuator and used only ALM neurons for this study. In all cases, this variation in worm positioning leads to variation in the size of the effective stimulus. To ensure that all animals received a deforming stimulus, we limited our analysis to animals whose TRNs were deformed enough to observe visually during the experiment.

Mitochondria as fiducial markers for inferring strain

We used fluorescent protein-tagged mitochondria as fiducial markers to measure strain, an approach that uses particle tracking with large (~1μm), immobile mitochondria in the TRNs (Sure et al., 2018) serving as natural fiducial markers. We imaged mitochondria position before

121 and after mechanical stimulation (Figures 1B and 1C). Next, we used the displacement between
122 adjacent mitochondria to quantify one-dimensional mechanical strain along the long axis of the
123 TRN (Figure 1D) according to: $\varepsilon = \Delta L/L_0$, where L_0 is the resting, undeformed length of an
124 object, and ΔL is the change in length of the object when deformed. For clarity, we refer to this
125 as longitudinal strain. As shown in Figure 1, mitochondria adjacent to the actuator moved more
126 than those anterior and posterior to the actuator (Figures 1B and 1C) and the inferred strain was
127 greatest near the center of the actuator (Figure 1D). This method enables direct observation of
128 touch-evoked strain in *C. elegans* TRNs in a single dimension aligned with the TRN's longest
129 dimension.

130 We note that this method is not suitable for detecting shear strain or bending strain. To
131 derive these measurements, we would need to detect angular changes (shear) or relative position
132 (bending) of the mitochondria within the TRNs. Given that the diameter of each mitochondrion
133 is only ~100 nm and the TRN is diameter is not much larger than this (200-300 nm, see Figure
134 3C, Cueva et al., 2007), such movements cannot be resolved because these objects are similar in
135 size to the estimated lateral resolution of 254 nm and axial resolution of 632 nm of our imaging
136 system. What about strain in directions orthogonal to the long axis of the TRN dendrite?
137 Although our image stacks contain three-dimensional position data (Figures 2A and 2B), the
138 initial distance between adjacent pairs of mitochondria in the *x* and *z* directions is small
139 compared to the resulting displacement. Thus, measurement resolutions lead to large
140 uncertainties in the strain calculation for these dimensions. Both limitations can be attributed to
141 the confinement of the mitochondria within the narrow caliber of the TRN and the fact that the
142 TRNs lie primarily within a single focal plane. Thus, the size of mitochondria, the geometry of
143 the TRNs and the optical resolution of the spinning-disk confocal limit this measurement to one-
144 dimensional strain along the *y*-dimension that traces the main axis of the TRN.

145

146 *Local indentation induces local mechanical strain in TRNs*

147 Next, we estimated the spatially averaged distribution of touch-induced strain in the
148 TRN. The mitochondria are sparsely distributed in the TRN and strain is a pairwise measurement
149 between adjacent mitochondria, so our strain measurements result in a series of discontinuous
150 step functions for a single trial rather than a smooth curve (Figure 1D). Each segment of the plot

151 indicates the average strain between two markers, so the maximum local strain on each interval
152 may be larger than our measured strain. The average distance between mitochondria in control
153 *jsIs1073* animals was 26 µm (min: 5 µm; max: 64 µm) and we were able to analyze an average
154 of 8.9 intervals per trial (Table S1). To obtain averages across trials, we plotted deformation
155 against position in the longitudinal or *y* direction, fit this profile with a Gaussian function and
156 defined the position of the maximum as the center of the actuator and *y*=0. (see dotted line in
157 Figure 1C). In this coordinate system, positions anterior to *y=0* are negative and positions
158 posterior to *y=0* are positive. Finally, we determined the average strain at each longitudinal
159 position along the neurite across actuation trials (see Figure 2C). Note that the average strain is
160 both larger and noisier for anterior (negative) positions. This is likely to reflect the fact that the
161 head is less constrained in the microfluidic channel than other parts of the body and suggests that
162 displacement and strain on the anterior side of the actuator include both touch- and movement-
163 induced mechanical strain on the neuron.

164 As expected, strain at the center of the actuator (*y=0*) increases with TRN deformation
165 (Figure 2D), but the dependence on TRN deformation was weak. The observed, but modest
166 variation in TRN deformation arises from two aspects of our method. First, because the actuator
167 is fixed to the surrounding material of the device on all sides, its center is the location of
168 maximum deformation. Second, although most animals are trapped with either their left or right
169 side in contact with the coverslip at the bottom of the device, some are rotated along their
170 anterior-posterior axis such that the position of the imaged TRN varies with respect to the
171 actuator (Figure 2A). Thus, the average strain induced between the pair of mitochondria at the
172 center of the actuator was 0.031±0.005 (mean ± SEM, n = 61 trials, N=15 animals) in transgenic
173 *jsIs1073* TRN neurons. Although additional studies exploring a wider range of deformations will
174 be needed to determine the nature relationship between TRN deformation and strain, to our
175 knowledge, these are the first *in vivo* measurements of touch-induced longitudinal strain in touch
176 receptor neurons, and they link local body indentation to local cellular deformation.

177

178 *Do tagged mitochondria affect TRN function?*

179 We used classical touch assays to address this question (Chalfie et al., 2014; Nekimken et
180 al., 2017b) by measuring touch sensitivity in wild-type (N2) and transgenic worms carrying the

181 transgenic mitochondria marker, *jsIs1073*. In blinded assays of three independent cohorts of 25
182 animals for each genotype, wild-type and *jsIs1073* animals had touch response rates of 0.869 and
183 0.865, respectively. The difference between the means was 0.00667 [95% CI (-0.0347, 0.048)].
184 Thus, the *jsIs1073* transgene does not decrease touch sensitivity.

185

186 *Selected ECM mutants and their touch sensation and anatomical phenotypes*

187 Having measured touch-induced mechanical strain in control TRNs, next we measured
188 longitudinal strain in four existing ECM mutants: *him-4(e1267), mec-1(e1738)*, *mec-1(e1066),*
189 and *mec-5(u440).* One of these mutants, *him-4(e1267),* has a partial defect in touch-sensitivity,
190 and the others are touch-insensitive (Du et al., 1996; Emtage et al., 2004; Vogel and Hedgecock,
191 2001). We reproduced these previous results using a ten-touch assay (Table 1). Whereas *him-4*
192 mutants retain MEC-4 puncta that are grossly wild-type, TRN neurites in *mec-1* and *mec-5*
193 mutants lack prominent MEC-4 puncta (Emtage et al., 2004). In *him-4* and in *mec-1(e1738)*
194 mutants analyzed here, the ALM and PLM neurons are displaced from their normal body
195 position near the lateral midlines and are not properly embedded in the epidermis (Emtage et al.,
196 2004; Vogel and Hedgecock, 2001). This effect is inferred to arise from a defective TRN-ECM
197 attachment (Vogel and Hedgecock, 2001). Consistent with this idea, the electron-dense ECM is
198 not detected in *mec-1* mutants (Chalfie and Sulston, 1981). Analyzing these four mutants enables
199 us to evaluate the relationship, if any, between touch-induced longitudinal strain and three other
200 phenotypes: behavioral responses to touch, the distribution of MEC-4 puncta, and TRN-ECM
201 attachment.

202 The *him-4* gene encodes hemicentin, a conserved ECM protein that is rich in Ig and EGF
203 domains and is expressed by body wall muscles (Vogel and Hedgecock, 2001). The *him-4* locus
204 is >30 kb, which complicated determination of the molecular defect encoded by *e1267* using
205 classical sequencing methods. We used whole-genome sequencing to circumvent this limitation
206 and found that *e1267* encodes a single base indel in the third intron of the *him-4* gene,
207 introducing a shift in the reading frame of the encoded protein (Figure S1). A second
208 polymorphism was detected in the intron following the 48th exon. Thus, the *e1267* allele is a null
209 allele and animals carrying this mutant are likely to lack the HIM-4 protein. The *mec-1* gene
210 encodes a large secreted protein rich in kunitz-like domains, is expressed by the TRNs, and many

211 alleles of this gene were found in forward genetic screens for touch-insensitive animals (Chalfie
212 and Au, 1989; Chalfie and Sulston, 1981). The *e1066* allele is a null and animals carrying this
213 allele are likely to lack the MEC-1 protein, whereas the *e1738* allele encodes a premature stop
214 codon and is proposed to express a truncated MEC-1 protein. Both *mec-1* mutants are touch
215 insensitive, but only *e1066* lacks proper TRN-ECM attachments (Emtage et al., 2004). *mec-5*
216 encodes an atypical collagen and, unlike *mec-1*, it is not made by the TRNs (Du et al., 1996).
217 Like other ECM mutants we analyzed here, the *u440* allele is null and *u440* mutants do not
218 express the MEC-5 protein. The TRN neurites in *mec-5* mutants are positioned near the lateral
219 midlines, but are less straight than they are in wild-type animals, meandering such that some
220 segments of the neurite are close to the muscle and other parts closer to the lateral midline
221 (Emtage et al., 2004).

222

223 *Touch-induced longitudinal strain in TRNs with ECM mutants*

224 To analyze transmission of mechanical energy from the skin in animals lacking proper
225 TRN-ECM attachment, we introduced the *jsIs1073* transgene into *him-4* and *mec-1* mutants and
226 applied mechanical stimuli to animals trapped in our pneumatic microfluidic device. Touch-
227 induced longitudinal mechanical strain in *him-4(e1267)* TRNs was indistinguishable from that
228 observed in control animals (Figure 3A, Table 2). Touch-induced longitudinal strain was
229 likewise similar to control in both *mec-1* mutants (Figure 3B) and in *mec-5* mutants (Figure 3C).
230 Figure 3D shows that the average longitudinal strain profiles for control, *him-4*, *mec-1*, and
231 *mec-5* mutants are similar across the entire 200 µm segment of the TRN neurite analyzed here.
232 Values for strain measured at the actuator center (y=0) had similar mean values and distribution
233 for all genotypes tested (Figure 4A) and estimation graphics (Ho et al., 2019) indicate that the
234 mean values for all genotypes are not different than control values (Figure 4B). Except for *mec-5*
235 mutants, the number of mitochondria available for tracking and the average distance between
236 mitochondria was similar in control transgenic and mutant animals (Table S1). *mec-5* mutants
237 had fewer, more widely spaced mitochondria than control animals, an effect would be expected
238 to impair the spatial resolution of longitudinal strain measurements. Collectively, these findings
239 suggest that neither severe nor mild defects in TRN-ECM attachment play a significant role in
240 the generation of touch-induced longitudinal mechanical strain at steady-state. Future studies

241 and techniques will be needed to resolve dynamic changes in local strain that are expected to
242 occur on the millisecond timescale of MEC-4-dependent MeT channel activation.

243

244 **Discussion**

245 Using mitochondria as natural fiducial markers in *C. elegans* TRNs, we showed for the
246 first time that body indentation sufficient to activate the TRN causes an increase in longitudinal
247 strain. The magnitude of this strain increases with TRN displacement. In wild-type animals, the
248 touch-induced strain closest to the point of maximum indentation was roughly 3% (Figure 3,
249 Table 2). This change in strain is unlikely to damage these sensory neurons, since they are
250 subjected to mechanical strain on the order of 40% during locomotion (Krieg et al., 2017; Krieg
251 et al., 2014). Such global changes in strain are too slow to activate the TRNs (Eastwood et al.,
252 2015; Katta et al., 2019).

253 The 3% strain we measured may be a lower bound on the true value for longitudinal
254 strain. Simulations predicted an elongated strain field with a peak value of 12% for longitudinal
255 strain (Sanzeni et al., 2019). Unlike our measurements, which used a wide (50µm), flexible
256 PDMS membrane to indent the worm's body and have limited spatial resolution, the simulations
257 employed a stiff spherical bead (10µm diameter) to deliver touch stimuli and a continuous
258 deformation function. The simulations (Sanzeni et al., 2019) predict strains are present in the
259 other two dimensions (along the direction of the stimulus and tangential to the circumference of
260 the worm at the point of the stimulus). Due to the nature of our measurement, however, we were
261 only able to measure one-dimensional strain along the length of the TRN. Nevertheless, these
262 measurements of touch-induced strain can be incorporated into future models of *C. elegans* touch
263 sensation to improve understanding of the mechanical state of the TRN and mechano-sensitive
264 ion channel complex upon touch stimulation.

265

266 *Origins of mechanical coupling between the skin surface and somatosensory neurons*

267 We tested the idea that strain transmission would depend on TRN-ECM attachment, be
268 correlated with impaired touch sensation, and be independent of the proper distribution of
269 MEC-4 channels. To our surprise, we found that touch-induced longitudinal mechanical strain

270 was similar in control TRNs and all ECM mutants tested here, including the *him-4(e1267)* and
271 *mec-1(e1066)* mutants exhibiting severe defects in TRN-ECM attachments. Thus, touch-induced
272 longitudinal strain we observed in the ALM neurons is independent of their attachment to other
273 tissues or the expression of ECM proteins MEC-1 and MEC-5, at least at steady state.

274 This finding implies that mechanical coupling between the skin and sensory neurons
275 persists in mutants with ECM defects. Friction is one alternative source of mechanical coupling
276 between TRNs and surrounding tissues. In this scenario, all of the worm's tissues are compacted
277 together by a high hydrostatic pressure and this would elevate friction between tissues. Further
278 compression applied to the outside of the worm during touch stimulation could lead to stiffening
279 of the worm's body that might be caused by internal structures jamming together (Gilpin et al.,
280 2015). When we and others immobilize worms in microfluidic devices, we fabricate channels
281 small enough to apply gentle compressive forces that the worm cannot overcome. As a result, the
282 worm is compressed on all sides except the nose and tail when in the microfluidic trap,
283 potentially jamming the TRNs against surrounding tissues and further increasing friction.
284 Another possibility is that the generation of touch-induced local mechanical strain is dominated
285 by the cytoskeleton. In support of this idea, mutations that disrupt the expression of MEC-12 α-
286 tubulin and MEC-7 β-tubulin decrease mechanoreceptor currents and increase stimulus
287 amplitude needed to activate these currents (Bounoutas et al., 2009; O'Hagan, 2005). Additional
288 experimental work and methods with improved spatial and temporal resolution will be needed to
289 differentiate among these possibilities.
290

291 *Spatial and temporal resolution of mechanical strain transmission*

292 The spatial resolution of our strain measurements is limited by the average distance
293 between adjacent, immobile mitochondria, which was 26μm (Table S1). Thus, this method may
294 lack sufficient spatial resolution to detect micro- or nanoscale variations in mechanical strain
295 transmission at steady state. The spatial resolution of strain measurements could be improved by
296 using more closely spaced fiducial markers. In principle, MEC-4 channels (with an average
297 spacing of 2-3 μm) tagged with a very bright fluorescent protein would provide a ten-fold
298 increase in resolution. Independent of potential improvements in spatial resolution, the present
299 approach is limited to steady-state measurements because our volume imaging rate is low (15

300 seconds per stack). In this regard, it is important to note that wild-type *C. elegans* TRNs are
301 preferentially activated mostly by high-velocity stimuli (Eastwood et al., 2015; Katta et al., 2019;
302 Nekimken et al., 2017a; Suzuki et al., 2003). Temporal resolution could be improved using other
303 imaging techniques enabling rapid acquisition of imaging volumes. If volumes could be acquired
304 at 20 Hz or faster, it would possible to observe mechanical strain in a 10 Hz buzz stimulus that
305 we previously used to activate the TRNs (Nekimken et al., 2017a).

306 *Conclusion*

307 We performed the first *in vivo* measurements of touch-induced mechanical strain in *C.*
308 *elegans* TRNs. We used mechanically stable mitochondria in the TRNs as natural fiducial
309 markers to observe deformation of the TRN and found that local touch stimuli applied in a
310 microfluidic device induces local strain in the TRN. Defects in the ECM surrounding the TRN
311 did not alter the steady-state mechanical strain in the TRN, suggesting that explicit attachments
312 are not necessary for deformation of the TRN and that the bulk properties of tissues are sufficient
313 to sustain significant mechanical energy transfer from the skin surface to the embedded neurons.
314 In light of the temporal limitations of our measurements, however, we cannot exclude the
315 possibility that TRN-ECM attachments contribute to dynamic aspects of mechanical strain
316 transmission. Collectively, these findings provide an empirical basis for the idea that mechanical
317 stimuli applied to the skin stretch embedded sensory neurons that may be shared by the sensory
318 neurons that innervate the skin and other tissue in mammals.
319

Methods and Materials

Nematode strains

For all experiments measuring mechanical strain, we used animals carrying *jsIs1073* [mec-7p::TagRFP-mito::CBunc-119], a transgene that drives expression of TagRFP in the mitochondria in the TRNs (Zheng et al., 2014), alone or together with ECM mutants (Table 3). We relied on visualization of the *jsIs1073* transgene and behavioral phenotypes (for *mec* genes) or anatomical defects (for *him-4*) to perform genetic crosses. We used gene sequencing to verify the presence of ECM mutants in all strains created for this study. The primer pairs we used to amplify the relevant segments of each gene are:
mec-1(e1066): Forward–catcttccacgccgcaaagtc, Reverse—aatcctctctgccctcatgttcc
mec-1(e1738): Forward—tcacagtcagacgtgcctcg, Reverse—cattgcctcacaccaacttccac
mec-5(u444): Forward—cagaatactatgtacgtaacttgggatc; Reverse—ctcatgggtacgcaaatgatactc
him-4(e1267): Forward—tttcgtgatgactggtgactgtgg; Reverse—ttaaagtcaacagcaccgtgacc

Immobilization and mechanical stimulation with a pneumatic microfluidics device

To provide a repeatable mechanical stimulus that is compatible with imaging the mitochondria of the TRN, we used a microfluidic device made of the transparent elastomer PDMS for simultaneous mechanical stimulation and imaging of *C. elegans* (Nekimken et al., 2017a). Using a pressure controller (Elveflow OB1), we applied 300 kPa of pressure to one of the device's actuators to create a mechanical stimulus. We fabricated and operated devices designed for use with young adult worms as described in our previous work (Fehlauer et al., 2018; Nekimken et al., 2017a). Because worms immobilized in this trap are uniformly and partially deformed by the channel, we refer to this as the rest configuration.

Sample preparation and inclusion criteria

We performed all experiments using young adult animals that were synchronized by hypochlorite treatment (Stiernagle, 2006) and cultured for three days on NGM agar plates seeded with OP50 bacteria for food. We transferred animals from the agar plates with a platinum wire

349 pick to a drop of imaging medium (see below) in a small Petri dish. After using the pick to push
350 away large particles that might clog the microfluidic device, we aspirated worms into
351 polyethylene tubing (PE50, Intramedic™ brand, Becton-Dickson) with a syringe and connected
352 the tubing to the device's inlet. For each trial, we pushed a worm into the trap channel using the
353 syringe and then evaluated whether to use this worm for an experiment based on our inclusion
354 criteria. We included animals that fit in the microfluidic trap with minimal movement and could
355 be ejected through the narrow opening at the head of the trap. When performing experiments
356 with *him-4* mutants, we chose animals whose gross morphology was wild-type and avoided
357 animals whose intestines were everted. In all cases, we only acquired images from animals
358 whose ALM neurons were oriented adjacent to the mechanical actuation channels.

359 To improve image quality by reducing reflections generated by the walls of the
360 microfluidic trap, we designed a non-toxic imaging medium with a refractive index similar to
361 PDMS (1.4). The imaging medium was a 70%:30% (vol:vol) mixture of physiological saline
362 and iodixanol (Optiprep™, Sigma-Aldrich), a non-toxic density-gradient medium (Boothe et al.,
363 2017). We used the same physiological saline as that used for electrophysiological recordings
364 from *C. elegans* neurons (O'Hagan et al., 2005), which contains (in mM): NaCl (145), KCl (5),
365 $MgCl_2$ (5), $CaCl_2$ (1), and Na-HEPES (10), adjusted to a pH of 7.2 with NaOH. The imaging
366 medium has an osmolality of 300-325 mOsm (Fiske Micro-Osmometer Model 210), so it does
367 not cause large osmotic shocks to *C. elegans*. By contrast with other fluids we tested (e.g.
368 glycerol, halocarbon oil), this medium has a viscosity that appeared to be similar to that of
369 physiological saline.

370

371 *Image acquisition*

372 Although the mechanical stimulus is mostly in the horizontal direction, there is enough
373 deformation in the z-direction to move the neuron out of plane during stimulation in some cases.
374 In initial experiments with a traditional epifluorescence microscope, the mitochondria often
375 moved out of focus during stimulation due to movement in the z-direction. To account for this
376 problem, we used a spinning disk confocal microscope (Nikon TiE, Yokogawa CSU-X1,
377 40x/NA 1.4 oil objective, and Photometrics Prime95B sCMOS camera) to acquire z-stacks,
378 which provided adequate resolution in the z-direction.

379 For each trial, we acquired eleven (11) z-stacks containing the neuron of interest, with
380 300 kPa of pressure applied during the even-numbered stacks, and 0 kPa applied during the odd-
381 numbered stacks. We started acquisition of a stack every 15 seconds, although the time to
382 acquire each given stack was approximately 12 seconds. The exact time varied depending on the
383 height of the z-stack, which was manually set to accommodate observed motion in the z direction
384 during the test actuation. During the short delay between acquisition of stacks, we toggled the
385 applied pressure.
386
387 *Image analysis*

388 To detect the mitochondria, we used a particle-tracking algorithm implemented in Python
389 (Allan et al., 2018), based on work by Crocker and Grier (Crocker and Grier, 1996). Briefly, the
390 algorithm involves applying a spatial band pass filter, finding peaks, refining the position of
391 peaks by finding their center of mass, and linking particles across timepoints into trajectories. In
392 some stacks, the algorithm failed to detect the mitochondria because they were too close to the
393 top or bottom of the stack, were not bright enough, overlapped with the mitochondria of another
394 TRN, or were blurred due to the motion of the worm. We discarded all stacks subsequent to a
395 stack where the image processing failed, because the strain measurement requires comparison to
396 a previous stack. Additionally, not all of the stacks from each trial were usable, since the
397 fluorophores bleached over time. As a result, not all actuation events yielded strain
398 measurements (see Supplementary Figure S2).

399 Due to variability across trials, we manually selected a region of interest around the TRN
400 and tuned parameters in the particle tracking algorithm. Primarily, we changed the minmass
401 threshold, which filters out particles where the sum of pixel values within the boundaries of the
402 particle is below the chosen threshold, and the search radius for the linking step, which specifies
403 how far a particle can travel between timepoints and still be identified as the same particle. Less
404 frequently, we changed the cutoff size for the bandpass filter or the brightness percentile
405 threshold, which sets a minimum value for the brightest pixel in a particle as a percentile of the
406 brightness of pixels in the image. We tuned these parameters until the particles found and linked
407 included only particles along the location of the neuron and not autofluorescent spots.
408 Supplemental Figure S3 shows the range of parameters we used.

409

410 *Touch assays*

411 To test the touch-sensitivity of the mutants used in our strain transmission experiments,
412 we performed touch assays by lightly stroking an eyebrow hair across the body of a worm and
413 scoring its behavioral response (Goodman, 2006). For each session of touch assays, we tested 25
414 worms from a plate, performing 10 touches per worm. We performed the touch assays blinded
415 with respect to genotype. For each touch event, we counted a response consisting of reversing
416 direction or speeding up to move away from the stimulus as a positive response.

417

418 *Whole-genome sequencing of* him-4(e1267)

419 Our whole-genome sequencing protocol involved four sub-protocols: 1) DNA extraction, 2)
420 sequencing library preparation, 3) sequencing, and 4) analysis. We isolated DNA from CB1267
421 *him-4(e1267) X* animals with a phenol chloroform isoamyl alcohol (PCI) extraction. First, we
422 washed worms off a mostly starved plate using M9 buffer, rinsed the animals twice in M9 buffer,
423 resuspended them in EN buffer (0.1M NaCl and 20 mM EDTA), removed the supernatant, and
424 flash-froze the sample in liquid nitrogen. Next, we added 450 µL of worm lysis buffer (0.1 M
425 TRIS pH 8.5, 0.1 M NaCl, 50 mM EDTA, and 1% SDS) and 40 µL of proteinase K (10 mg/ml)
426 to 50 µL of frozen worms and incubated at 62°C for 45 minutes, vortexing occasionally. Then,
427 we performed the PCI extraction in a phase lock gel tube (VWR) by adding 500 µL of PCI to the
428 sample, vortexing, spinning for 5 minutes at 10,000 rpm, and then collecting the upper phase.
429 We repeated the PCI extraction step, and then extracted twice using chloroform. We precipitated
430 the DNA by adding 40 µL of 5M sodium acetate and 1 mL of ethanol, spinning for 5 minutes at
431 10,000 rpm, removing the supernatant, washing in 70% ethanol, and resuspending in 50 µL of
432 TE buffer at pH 7.4.

433 We created a sequencing library according to manufacturer instructions (Nextera DNA
434 Library Prep Kit, Illumina). Briefly, this includes tagmentation of the DNA using the Illumina
435 Tagment DNA Buffer and Enzyme, clean-up of the tagmented DNA using a Zymo DNA Clean
436 and Concentrator Kit, PCR to add the library indices to the tagmented DNA, and PCR cleanup
437 by gel extraction using a Qiagen MinElute Kit. We did a quality control step to confirm that the
438 average length of DNA fragments was in the expected range of 300-500 bp using the Agilent

439 Bioanalyzer at the Stanford Protein and Nucleic Acid Biotechnology Facility. Sequencing was
440 completed on an Illumina NextSeq sequencer in the Stanford Functional Genomics Facility.

441 We analyzed the sequencing data using the computing cluster of the Stanford Center for
442 Genomics and Personalized Medicine. Briefly, we mapped reads using Bowtie2, used Picard to
443 sort reads, mark duplicates, and prepare read groups, then used GATK to select high quality
444 SNPs and INDELs, and SnpEff to annotate the results.

445

446 *Code availability*

447 Two kinds of data were analyzed using custom code: image analysis (Python,
448 https://github.com/anekimken/SSN_ImageAnalysis) and whole-genome sequence analysis
449 available (scripts, https://github.com/wormsenseLab/whole_genome_sequencing).

450

451 **Acknowledgments**

452 We thank Chloe Girard, Chantal Akerib, Melissa Pickett, and Anne Villenueve for the gift of
453 their training and assistance in whole genome sequencing; Michael Nonet for NM3573, the strain
454 with labeled mitochondria in the TRNs; Ehsan Rezeai for help with software testing; Michael
455 Lin for the loan of a spinning disk confocal for pilot experiments. Some of the experiments were
456 performed at Stanford core facilities, including the Cell Sciences Imaging Facility, Functional
457 Genomics Facility (funded in part by a Shared Instrumentation Grant, NIH S10OD018220), the
458 Genetics Bioinformatics Service Center, and the nano@Stanford labs (supported by the National
459 Science Foundation as part of the National Nanotechnology Coordinated Infrastructure under
460 award ECCS-1542152). This work was funded by an NIH fellowship to ALN (F31NS100318)
461 and grant to MBG (R35NS105092).

462

463 **References**

464 Allan, D.B., Caswell, T., Keim, N.C., van der Wel, C.M., 2018. trackpy: Trackpy v0.4.1.
465 doi:10.5281/ZENODO.1226458

466 Bewick, G.S., Banks, R.W., 2015. Mechanotransduction in the muscle spindle. Pflügers Arch. -
467 Eur. J. Physiol. 467, 175–190.

468 Boothe, T., Hilbert, L., Heide, M., Berninger, L., Huttner, W.B., Zaburdaev, V., Vastenhouw,
469 N.L., Myers, E.W., Drechsel, D.N., Rink, J.C., 2017. A tunable refractive index matching
470 medium for live imaging cells, tissues and model organisms. Elife 6.
471 doi:10.7554/eLife.27240

472 Bounoutas, A., O'Hagan, R., Chalfie, M., 2009. The Multipurpose 15-Protofilament
473 Microtubules in C. elegans Have Specific Roles in Mechanosensation, Current Biology.
474 doi:10.1016/j.cub.2009.06.036

475 Chalfie, M., Au, M., 1989. Genetic control of differentiation of the Caenorhabditis elegans touch
476 receptor neurons. Science (80-.). 243, 1027–1033.

477 Chalfie, M., Hart, A.C., Rankin, C.H., Goodman, M.B., 2014. Assaying mechanosensation.
478 WormBook.

479 Chalfie, M., Sulston, J., 1981. Developmental genetics of the mechanosensory neurons of
480 Caenorhabditis elegans. Dev. Biol. 82, 358–370. doi:10.1016/0012-1606(81)90459-0

481 Chalfie, M., Thomson, J.N., 1979. Organization of neuronal microtubules in the nematode
482 Caenorhabditis elegans. J. Cell Biol. 82, 278–289.

483 Chelur, D.S., Ernstrom, G.G., Goodman, M.B., Yao, C.A., Chen, L., O Hagan, R., Chalfie, M.,
484 O'Hagan, R., Chalfie, M., 2002. The mechanosensory protein MEC-6 is a subunit of the C.
485 elegans touch-cell degenerin channel. Nature 420, 669–673. doi:10.1038/nature01205

486 Cho, Y., Oakland, D.N., Lee, S.A., Schafer, W.R., Lu, H., 2018. On-chip functional
487 neuroimaging with mechanical stimulation in: Caenorhabditis elegans larvae for studying
488 development and neural circuits. Lab Chip 18, 601–609. doi:10.1039/c7lc01201b

489 Crocker, J.C., Grier, D.G., 1996. Methods of Digital Video Microscopy for Colloidal Studies. J.

490 Colloid Interface Sci. 179, 298–310. doi:10.1006/jcis.1996.0217

491 Cueva, J.G., Mulholland, A., Goodman, M.B., 2007. Nanoscale Organization of the MEC-4
492 DEG/ENaC Sensory Mechanotransduction Channel in Caenorhabditis elegans Touch
493 Receptor Neurons. J. Neurosci. 27, 14089–14098.

494 Du, H., Gu, G., William, C.M., Chalfie, M., 1996. Extracellular proteins needed for C. elegans
495 mechanosensation. Neuron 16, 183–194.

496 Eastwood, A.L., Sanzeni, A., Petzold, B.C., Park, S.-J., Vergassola, M., Pruitt, B.L., Goodman,
497 M.B., 2015. Tissue mechanics govern the rapidly adapting and symmetrical response to
498 touch. Proc. Natl. Acad. Sci. 112, E6955–E6963. doi:10.1073/pnas.1514138112

499 Emtage, L., Gu, G., Hartwieg, E., Chalfie, M., 2004. Extracellular proteins organize the
500 mechanosensory channel complex in C. elegans touch receptor neurons. Neuron 44, 795–
501 807.

502 Fehlauer, H., Nekimken, A.L.A.L., Kim, A.A.A.A., Pruitt, B.L.B.L., Goodman, M.B.M.B.,
503 Krieg, M., 2018. Using a microfluidics device for mechanical stimulation and high
504 resolution imaging of C. Elegans. J. Vis. Exp. 2018. doi:10.3791/56530

505 Gilpin, W., Uppaluri, S., Brangwynne, C.P., 2015. Worms under Pressure: Bulk Mechanical
506 Properties of C. elegans Are Independent of the Cuticle. Biophys. J. 108, 1887–1898.

507 Goodman, M., 2006. Mechanosensation. WormBook. doi:10.1895/wormbook.1.62.1

508 He, L., Gulyanon, S., Mihovilovic Skanata, M., Karagyozov, D., Heckscher, E.S., Krieg, M.,
509 Tsechpenakis, G., Gershow, M., Tracey, W.D., 2019. Direction Selectivity in Drosophila
510 Proprioceptors Requires the Mechanosensory Channel Tmc. Curr. Biol. 29, 945-956.e3.
511 doi:10.1016/j.cub.2019.02.025

512 Ho, J., Tumkaya, T., Aryal, S., Choi, H., Claridge-Chang, A., 2019. Moving beyond P values:
513 data analysis with estimation graphics. Nat. Methods. doi:10.1038/s41592-019-0470-3

514 Katta, S., Krieg, M., Goodman, M.B., 2015. Feeling Force: Physical and Physiological Principles
515 Enabling Sensory Mechanotransduction, in: Annual Review of Cell and Developmental
516 Biology. doi:10.1146/annurev-cellbio-100913-013426

517 Katta, S., Sanzeni, A., Das, A., Vergassola, M., Goodman, M.B., 2019. Progressive recruitment
518 of distal MEC-4 channels determines touch response strength in C. elegans. J. Gen. Physiol.
519 doi:10.1085/jgp.201912374

520 Krieg, M., Dunn, A.R., Goodman, M.B., 2014. Mechanical control of the sense of touch by β-
521 spectrin. Nat. Cell Biol. 16. doi:10.1038/ncb2915

522 Krieg, Michael, Dunn, A.R., Goodman, M.B., 2014. Mechanical control of the sense of touch by
523 β-spectrin. Nat. Cell Biol. 16, 224–233.

524 Krieg, M., Stühmer, J., Cueva, J.G., Fetter, R., Spilker, K., Cremers, D., Shen, K., Dunn, A.R.,
525 Goodman, M.B., 2017. Genetic defects in β-spectrin and tau sensitize C. Elegans axons to
526 movement-induced damage via torque-tension coupling. Elife 6. doi:10.7554/eLife.20172

527 McClanahan, P.D., Xu, J.H., Fang-Yen, C., 2017. Comparing Caenorhabditis elegans gentle and
528 harsh touch response behavior using a multiplexed hydraulic microfluidic device. Integr.
529 Biol. doi:10.1039/C7IB00120G

530 Nekimken, A.L., Fehlauer, H., Kim, A.A., Manosalvas-Kjono, S.N., Ladpli, P., Memon, F.,
531 Gopisetty, D., Sanchez, V., Goodman, M.B., Pruitt, B.L., Krieg, M., 2017a. Pneumatic
532 stimulation of C. elegans mechanoreceptor neurons in a microfluidic trap 17, 1116–1127.

533 Nekimken, A.L., Mazzochette, E.A., Goodman, M.B., Pruitt, B.L., 2017b. Forces applied during
534 classical touch assays for Caenorhabditis elegans. PLoS One 12.
535 doi:10.1371/journal.pone.0178080

536 O'Hagan, R., 2005. Components of a Mechanotransduction Complex in C. elegans Touch
537 Receptor Neurons: An in vivo Electrophysiology Study. Columbia University.

538 O'Hagan, R., Chalfie, M., Goodman, M.B., 2005. The MEC-4 DEG/ENaC channel of
539 Caenorhabditis elegans touch receptor neurons transduces mechanical signals. Nat.
540 Neurosci. 8, 43–50. doi:10.1038/nn1362

541 O'Toole, M., Lamoureux, P., Miller, K.E., 2015. Measurement of subcellular force generation in
542 neurons. Biophys. J. 108, 1027–1037. doi:10.1016/j.bpj.2015.01.021

543 Petzold, B.C., Park, S.-J., Mazzochette, E.A., Goodman, M.B., Pruitt, B.L., 2013. MEMS-based

544 force-clamp analysis of the role of body stiffness in C. elegans touch sensation. Integr. Biol.
545 (Camb). 5, 853–864. doi:10.1039/c3ib20293c

546 Phillips, J.B., Smit, X., Zoysa, N. De, Afoke, A., Brown, R.A., 2004. Peripheral nerves in the rat
547 exhibit localized heterogeneity of tensile properties during limb movement. J. Physiol. 557,
548 879–887. doi:10.1113/jphysiol.2004.061804

549 Ribeiro, A.J.S., Denisin, A.K., Wilson, R.E., Pruitt, B.L., 2016. For whom the cells pull:
550 Hydrogel and micropost devices for measuring traction forces. Methods 94, 51–64.
551 doi:10.1016/j.ymeth.2015.08.005

552 Sanzeni, A., Katta, S., Petzold, B., Pruitt, B.L., Goodman, M.B., Vergassola, M., 2019.
553 Somatosensory neurons integrate the geometry of skin deformation and
554 mechanotransduction channels to shape touch sensing. Elife 8, 1–44.
555 doi:10.7554/eLife.43226

556 Stiernagle, T., 2006. Maintenance of C. elegans. WormBook. doi:10.1895/wormbook.1.101.1

557 Sure, G.R., Chatterjee, A., Mishra, N., Sabharwal, V., Devireddy, S., Awasthi, A., Mohan, S.,
558 Koushika, S.P., 2018. UNC-16/JIP3 and UNC-76/FEZ1 limit the density of mitochondria in
559 C. elegans neurons by maintaining the balance of anterograde and retrograde mitochondrial
560 transport. Sci. Rep. 8, 8938. doi:10.1038/s41598-018-27211-9

561 Suslak, T.J., Jarman, A.P., 2015. Stretching the imagination beyond muscle spindles - stretch-
562 sensitive mechanisms in arthropods. J. Anat. 227, 237–242. doi:10.1111/joa.12329

563 Suzuki, H., Kerr, R., Bianchi, L., Frøkjær-Jensen, C., Slone, D., Xue, J., Gerstbrein, B., Driscoll,
564 M., Schafer, W.R., 2003. In vivo imaging of C. elegans mechanosensory neurons
565 demonstrates a specific role for the MEC-4 channel in the process of gentle touch sensation.
566 Neuron 39, 1005–1017.

567 Tao, L., Porto, D., Li, Z., Fechner, S., Lee, S.A., Goodman, M.B., Xu, X.Z.S., Lu, H., Shen, K.,
568 2019. Parallel Processing of Two Mechanosensory Modalities by a Single Neuron in C.
569 elegans. Dev. Cell 51, 617-631.e3. doi:10.1016/j.devcel.2019.10.008

570 Vaadia, R.D., Li, W., Voleti, V., Singhania, A., Hillman, E.M.C., Grueber, W.B., 2019.
571 Characterization of Proprioceptive System Dynamics in Behaving Drosophila Larvae Using

572 High-Speed Volumetric Microscopy. Curr. Biol. 29, 935-944.e4.
573 doi:10.1016/j.cub.2019.01.060

574 Vogel, B.E., Hedgecock, E.M., 2001. Hemicentin, a conserved extracellular member of the
575 immunoglobulin superfamily, organizes epithelial and other cell attachments into oriented
576 line-shaped junctions. Development 128, 883–894.

577 Zheng, Q., Ahlawat, S., Schaefer, A., Mahoney, T., Koushika, S.P., Nonet, M.L., 2014. The
578 Vesicle Protein SAM-4 Regulates the Processivity of Synaptic Vesicle Transport. PLoS
579 Genet. 10, e1004644. doi:10.1371/journal.pgen.1004644

580

581

582 **Figure Legends**

583

584 **Figure 1: Touch-induced mechanical strain measured using mitochondria as fiducial**
585 **markers in *C. elegans* TRNs *in vivo*.**

586 A) Brightfield image of worm in the microfluidic device. Scale bar 20 µm. B) Maximum
587 projection image of TRN mitochondria before (magenta) and during (green) mechanical
588 stimulus. Mitochondria that did not move appreciably appear white due to the overlap of
589 magenta and green. Image intensity and contrast was adjusted to improve visualization. Scale bar
590 20 µm. C) Displacement in the direction of actuation before (magenta) and during (green)
591 stimulation. The smooth line (green) is a Gaussian fit used to infer the center of actuator. D)
592 Distribution of touch-induced strain in the TRN for a single actuation trial.
593

Figure 2: Indentation induces local longitudinal strain in *C. elegans* TRNs.

A) Three-dimensional diagram the positioning of the worm in the microfluidics trap, the animal-centric coordinate system used to characterize strain, and the consequences of trapping animals in different orientations. TRN is red, and muscles are included in brown as visual aid. B) Touch-induced displacement in three dimensions. C) Touch-induced strain, anterior is to the left and posterior is to the right. $y=0$ is the center of the actuator. n=61 trials from N=15 worms. D) Mechanical strain at $y=0$ as a function of maximum neuron displacement. The line is a linear fit to the data: $\varepsilon = 0.0061x - 0.0067$, where ε is the strain and x is the maximum displacement. The shaded area indicates 95% confidence intervals of the fit. $R^2 = 0.04$.

607 **Figure 3: Touch-induced mechanical strain profiles are similar in control animals and**
608 **ECM mutants.**

609 A) Spatially averaged strain in control ALM neurons with normal TRN attachment (15 animals)
610 and *him-4(e1267)* with attachment defects (16 animals). The data for control animals are the
611 same data as Figure 2. B) Spatially averaged strain in *mec-1* mutants. 14 independent animals for
612 *mec-1(1066)* and 16 animals for *mec-1(e1738)*. C) Spatially averaged strain in *mec-5(u444)*
613 mutants (17 animals). D) Overlay of all spatially averaged strain profiles. Smooth lines are the
614 averages across all trials and shaded areas show the error (95% confidence intervals). One ALM
615 neuron tested in each animal.
616

Figure 4: Strain at the center of the actuator is similar in control animals and ECM mutants

A) Strain at the center of the actuator. Each point is the result of a single trial. The vertical lines next to the swarm plots indicate the median and quartiles of the data. Data collected from 15, 16, 14, 16, and 17 animals (left to right). B) Difference in the mean strain between control and each mutant with a bootstrapped resampled distribution of the data. Estimation plots generated using the DABEST plotting package (Ho et al., 2019).

624

625 **Table 1: Touch sensitivity of ECM mutants.**

626

Genotype	Response probability	Mean difference from control	95% confidence interval of mean difference
control	0.742		
him-4(e1267)	0.527	-0.215	(-0.275, -0.163)
mec-1(e1066)	0.083	-0.659	(-0.698, -0.619)
mec-1(e1738)	0.237	-0.505	(-0.551, -0.461)
mec-5(u444)	0.208	-0.534	(-0.580, -0.487)

627 All mutants we tested were less sensitive to touch than control animals; effect size was smallest
628 for *him-4(e1267)* and largest for *mec-1(e1066)*. All strains tested contained the transgene
629 *jsIs1073* that tags mitochondria in the TRNs with RFP. *N*=100 worms for each genotype, tested
630 in four independent cohorts of 25 blinded to genotype.

631

632

633

634 **Table 2: Touch-evoked longitudinal strain in the TRNs as a function of genotype.**

635

Genotype	Mean strain ± SEM	Mean difference from control	95% confidence interval of mean difference	stimulation trials	animals
control	0.031 ± 0.005			61	15
him-4(e1267)	0.024 ± 0.005	-0.007	(-0.020, 0.007)	61	16
mec-1(e1066)	0.034 ± 0.007	0.003	(-0.012 0.022)	49	14
mec-1(e1738)	0.035 ± 0.005	0.004	(-0.009 0.018)	68	16
mec-5(u444)	0.026 ± 0.009	-0.005	(-0.028 0.013)	44	17

636 There was no detectable difference in the magnitude of the touch-evoked strain in control and

637 ECM mutant animals.

638

639 **Table 3: *C. elegans* strains**

640

Strain Name	Genotype	Source
N2 (Bristol)	wild-type	CGC
NM3573	*jsIs1073*	(Zheng et al., 2014)
GN885	*jsIs1073;him-4(e1267)*	this study
GN886	*jsIs1073;mec-1(e1066)*	this study
GN887	*jsIs1073;mec-1(e1738)*	this study
GN906	*jsIs1073;mec-5(u444)*	this study

641

642

643

644

645

646

647

648

Figure S1: *him-4(e1267)* is likely to be a null allele. A) Map of *him-4* with *e1267* allele annotated. B) Close-up of insertion in sequence as indicated by dotted lines in Panel A. C) Sequences of both Indels found by sequencing. The first indel is likely to cause the null phenotype because it causes a frameshift in an early exon, whereas the second indel is in a later intron.

Figure S2: Quality control for image (z) stacks as a function of genotype. Eleven (11) image stacks were collected from each TRN analyzed for touch-induced strain. This plot shows the number of stacks that passed quality for each experiment. Note: The final stack was not used as it was acquired in the resting configuration and could not be compared to a subsequent stack collected in the indented configuration.

Figure S3: We tuned parameters of the particle tracking algorithm to account for variability across images.

664 **Table S1: Average number of detected mitochondria and distance between adjacent**
665 **detected mitochondria as a function of genotype.**
666

Number of mitochondria					
Genotype	Mean number ± SEM	Mean difference from control	95% confidence interval of mean difference	Minimum	Maximum
Control	8.9 ± 0.6			5	15
him-4(e1267)	9.1 ± 0.5	0.2	(-1.5, 1.6)	6	13
mec-1(e1066)	8.8 ± 0.5	-0.1	(-1.7, 1.5)	6	13
mec-1(e1738)	8.9 ± 0.5	0.01	(-1.6, 1.5)	6	15
mec-5(u444)	7.2 ± 0.5	-1.7	(-3.3, -0.3)	5	12
Distance between adjacent mitochondria					
Genotype	Mean distance ± SEM (μm)	Mean difference from control (μm)	95% confidence interval of mean difference (μm)	Minimum (μm)	Maximum (μm)
Control	26.0± 0.4			5.4	63.7
him-4(e1267)	27.3±0.4	1.4	(-2.0, 4.8)	5.0	76.1
mec-1(e1066)	27.0±0.5	1.0	(-2.6, 4.7)	5.3	65.1
mec-1(e1738)	26.9±0.4	0.9	(-2.4, 4.3)	6.0	64.1
mec-5(u444)	31.1±0.6	5.2	(1.2, 9.3)	5.5	84.1

667
668 The number of detected mitochondria and distance between adjacent mitochondria in the ALM
669 neurons was similar in control and the ECM mutants, except for *mec-5(u444)* which had fewer
670 detected mitochondria and larger distances between adjacent mitochondria, on average. Number
671 of animals is the same as Table 2.
672
673

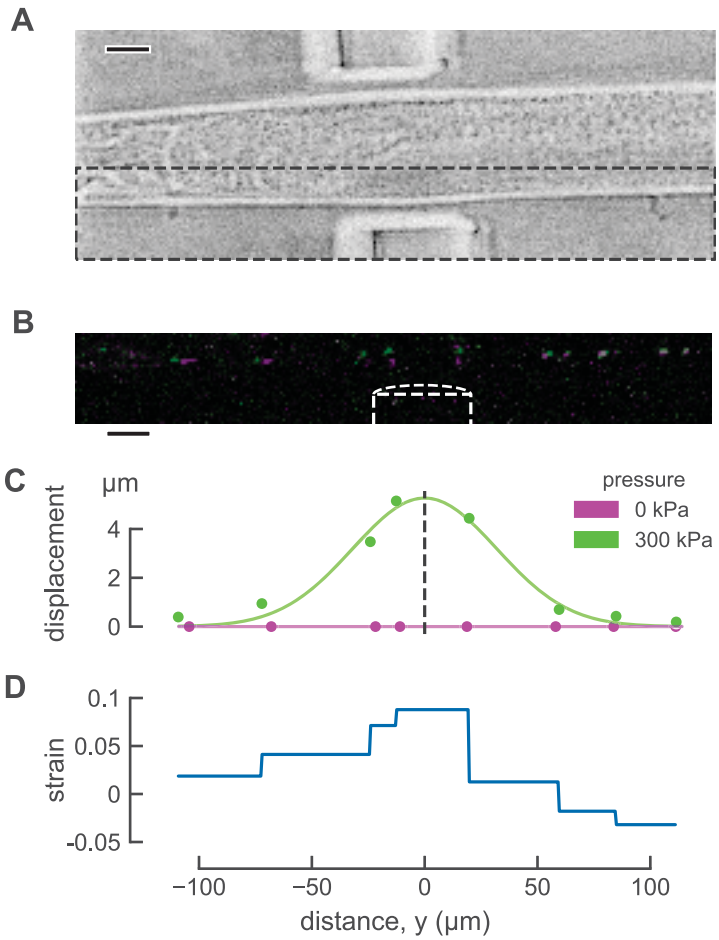
A
B
C
μm
displacement
4
2
0
pressure
0 kPa
300 kPa
D
0.1
0.05
0
-0.05
strain
−100
−50
0
50
100
distance, y (μm)

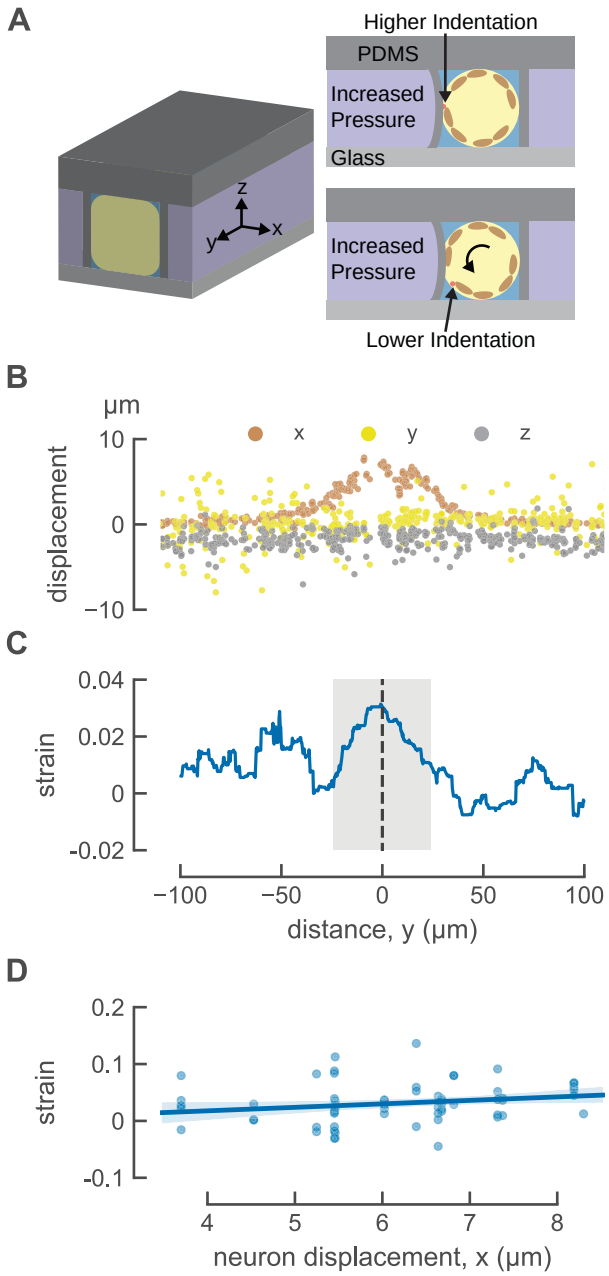
A
Higher Indentation
PDMS
Increased Pressure
Glass
z
y
x
Increased Pressure
Lower Indentation
B
µm
x
y
z
displacement
10
0
−10
C
strain
0.04
0.02
0
-0.02
−100
−50
0
50
100
distance, y (µm)
D
strain
0.2
0.1
0
-0.1
4
5
6
7
8
neuron displacement, x (µm)

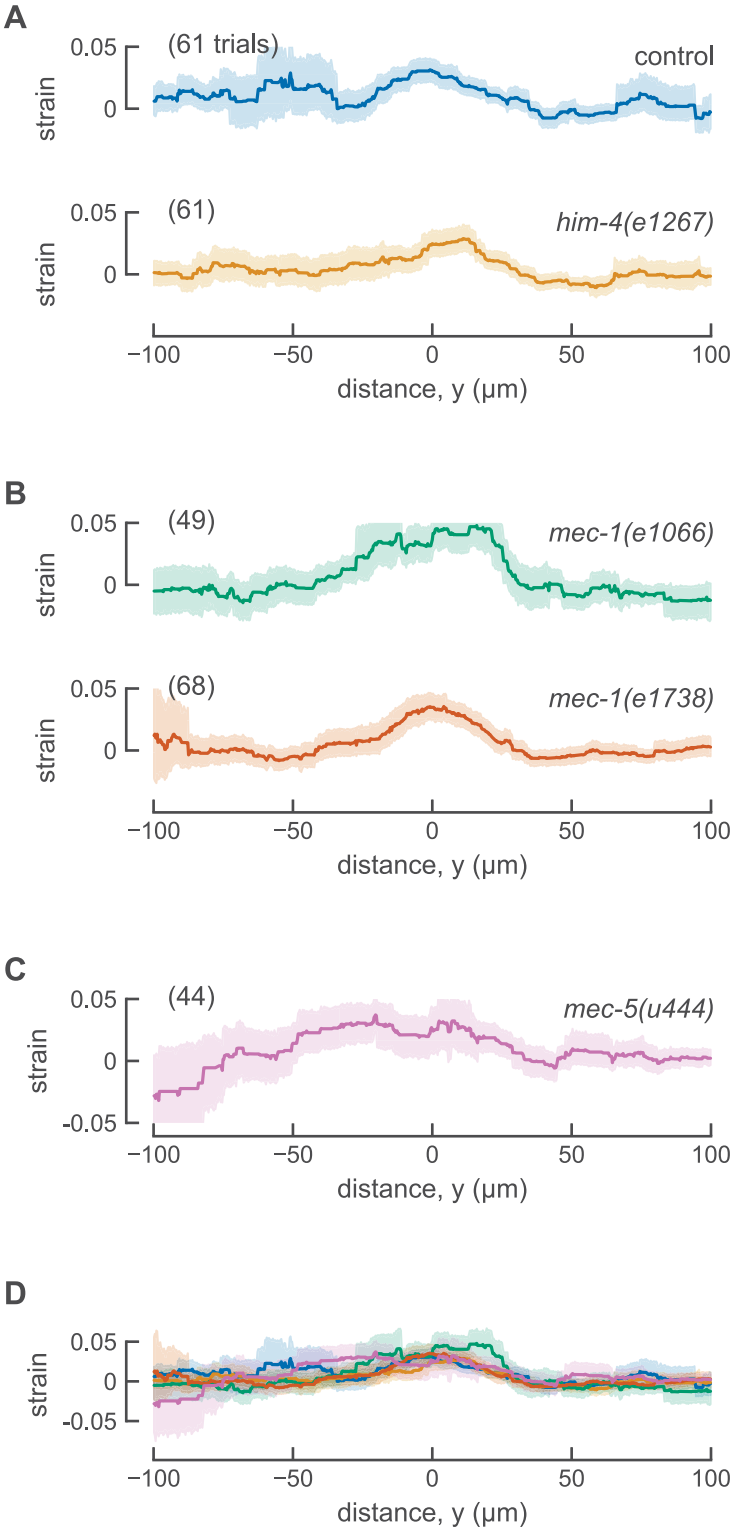
A
(61 trials)
control
0.05
0
strain
(61)
him-4(e1267)
0.05
0
strain
−100
−50
0
50
100
distance, y (μm)
B
(49)
mec-1(e1066)
0.05
0
strain
(68)
mec-1(e1738)
0.05
0
strain
−100
−50
0
50
100
distance, y (μm)
C
(44)
mec-5(u444)
0.05
0
-0.05
strain
−100
−50
0
50
100
distance, y (μm)
D
0.05
0
-0.05
strain
−100
−50
0
50
100
distance, y (μm)

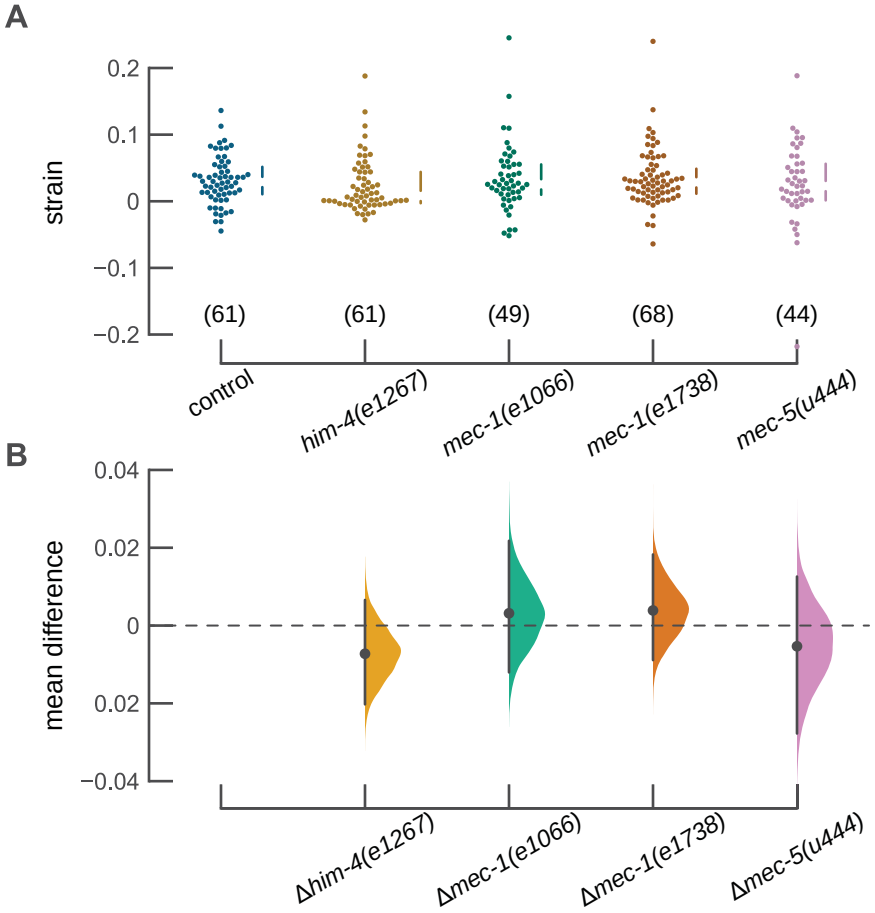
A
strain
0.2
0.1
0
−0.1
−0.2
(61)
(61)
(49)
(68)
(44)
control
him-4(e1267)
mec-1(e1066)
mec-1(e1738)
mec-5(u444)
B
mean difference
0.04
0.02
0
0.02
−0.04
Δhim-4(e1267)
Δmec-1(e1066)
Δmec-1(e1738)
Δmec-5(u444)